Marginal turbulent state of viscoelastic fluids: A polymer drag reduction perspective

Xi and Bai (2016)

DOI: 10.1103/PhysRevE.93.043118

Li Xi and Xue Bai. Marginal turbulent state of viscoelastic fluids: A polymer drag reduction perspective. *Physical Review E*, 93:043118, 2016. doi: 10.1103/PhysRevE.93.043118

BibTeX Citation Entry

```
@article{XiPRE16,
  author = {Xi, Li and Bai, Xue},
  title  = {{Marginal turbulent state of
         viscoelastic fluids:  A polymer
         drag reduction perspective}},
  journal= {Physical Review E},
  volume = {93},
  pages  = {043118},
  year   = {2016},
}
```

PHYSICAL REVIEW E **93**, 043118 (2016)

Marginal turbulent state of viscoelastic fluids: A polymer drag reduction perspective

Li Xi[*] and Xue Bai

Department of Chemical Engineering, McMaster Universtiy, Hamilton, Ontario, Canada L8S 4L7

(Received 20 August 2015; revised manuscript received 28 January 2016; published 19 April 2016)

The laminar-turbulent (LT) transition of dilute polymer solutions is of great interest not only for the complex transition dynamics itself, but also for its potential link to the maximum drag reduction (MDR) phenomenon. We present an in-depth investigation of the edge state (ES), an asymptotic solution on the LT boundary, in viscoelastic channel flow. For given Re and simulation domain size, mean flow statistics of the ES do not vary with the introduction of polymers, proving that there is a region of turbulent states not susceptible to polymer drag reduction effects. The dynamics of the ES features low-frequency fluctuations and in the longer domains we studied it is nearly periodic with regular bursts of turbulent activities separated by extended quiescent periods. Its flow field is dominated by elongated vortices and streaks, with very weak extensional and rotational flow motions. Polymer stretching is almost exclusively contributed by the mean shear and polymer-turbulence interaction is minimal. Flow structures and the kinematics of the ES match hibernating turbulence, an MDR-like phase intermittently occurring in turbulent dynamics. Its observation now seems to result from recurrent visits to certain parts of the ES. The ES offers explanations for the existence and universality of MDR, the quantitative magnitude of which, however, still remains unsolved.

DOI: 10.1103/PhysRevE.93.043118

I. INTRODUCTION

The interaction of linear long-chain polymer molecules with flow turbulence has attracted immense interest since the 1940s, when it was first discovered that these additives, at extremely low levels of concentration [$O(10-100)$ weight parts per 10^6], can cause significant reduction in the turbulent friction drag [1–4]. The study of this polymer-induced drag reduction (DR) phenomenon largely boils down to two major problems [5]: the onset of DR and the maximum drag reduction (MDR) asymptote. The first problem in essence is about understanding how polymers affect turbulence and reduce its drag, based on which the onset point of DR can be predicted. It is now widely accepted that polymers suppress turbulent vortex motions, which redistributes the momentum to the flow direction [6–10], although the exact nature of this polymer-turbulence interplay is still under debate [1,5,11,12]. The gap in our understanding is especially manifested in the laminar-turbulent (LT) transition behaviors of dilute polymer solutions, where conflicting observations were made in experiments. From the aforementioned vortex-suppression effect, it would be intuitive to predict a delayed transition with the addition of polymers, i.e., turbulence occurring at higher Re than that in Newtonian fluids, which was indeed reported in many studies [13–15]. Meanwhile, early turbulence in polymer solutions has also been observed under certain conditions [16,17].

The problem of MDR is an even larger puzzle. With stronger polymer influence, through more effective polymer molecules or higher concentration, the level of DR normally increases. This trend, however, eventually saturates to an upper bound. Contrary to common intuition, the MDR asymptote is universal with respect to changing polymer solution properties: At given Re, the measured flow rate at MDR is the same regardless of the polymer species, molecular weight, or concentration. Mean velocity profiles at MDR were empirically fitted by Virk [2] to the logarithmic law formulation

$$U_m^+(y^+) = A^+ \ln y^+ + B^+, \tag{1}$$

with $A^+_{\text{Virk}} = 11.7$ and $B^+_{\text{Virk}} = -17.0$ across most of the domain. [In comparison, the Prandtl–von Kármán (PvK) logarithmic law of Newtonian turbulence with $A^+_{\text{PvK}} = 2.5$ and $A^+_{\text{PvK}} = 5.5$ [18] is only valid in a near-wall layer [19]; hereinafter, $+$ denotes quantities in turbulent inner scales (see Sec. II A).] Advancement in flow imaging and direct numerical simulation (DNS) techniques in the past two decades has further revealed that flow patterns at MDR are distinctively different from Newtonian turbulence [20–24]. Therefore, in highly elastic polymers solutions, turbulence does not completely vanish; instead, traditional turbulent states are replaced by a new type of turbulence whose mean flow is invariant with changing polymer properties.

Early theoretical attempts of explaining MDR focused on the length scale of polymer effects [2,25]. Despite their lack of physical details, these phenomenological theories offered important guidance for earlier DR research. However, as data have become increasingly available, contradictory evidence has emerged in both experiments and numerical simulations (see detailed discussions in [21,26]). On the other hand, the universality of MDR prompted the speculation that it may be associated with a class of weak or marginal turbulent states already existing in Newtonian flows but only become unmasked with high levels of polymer elasticity [3]. The assumption that marginal turbulent states cannot be further suppressed by polymers has also led to phenomenological models predicting MDR mean flow statistics [27,28]. Evidence for this hypothesis was only discovered recently, when intermittent transitions between strong active turbulence and weak hibernating turbulence were first reported in DNS [26,29,30]. Many similarities, both qualitative and quantitative, are found between hibernating turbulence and MDR. As fluid elasticity increases, the transition to hibernating states becomes much

---

[*] Corresponding author: xili@mcmaster.ca

more frequent, resulting in them taking up a larger proportion of the overall statistics or a flow more dominated by features of MDR. Similar MDR-like Newtonian turbulent states were also found in transitional turbulence [31] and boundary layer flow [32]. Traveling-wave solutions that closely resemble hibernating turbulence and MDR were found recently in Newtonian channel flow and DNS trajectories were shown to visit these states intermittently [33], offering the strongest support yet for this dynamical perspective of MDR.

In search of this marginal state, one needs to consider the layout of the dynamical state space: two basins of attraction, the laminar state and normal turbulence, are separated by a boundary or ridge termed the edge of chaos [34,35]. Dynamical trajectories initiated from one side of the boundary are destined for the turbulent basin and those from the other will decay to the laminar state. Trajectories starting on this boundary head to neither of the basins. They move along this boundary and asymptotically approach an edge state (ES), a saddle point (consisting of traveling waves and relative periodic orbits [36]) on this ridge that is pivotal to the LT transitions [37]. To perturb a laminar flow into turbulence, the disturbance must be strong enough to overpass the ES. In this sense, the ES is the marginal state defining the weakest form of turbulence that can be sustained. In an encouraging recent development [38], it was found, at least for one Re and domain size, that introducing drag-reducing polymers does not change the mean flow measurements of the ES. Considering the unique positioning of the ES in the state space, this suggests that between the laminar and turbulent basins, there is a band of states not susceptible to the drag-reducing effects, which would explain why MDR must exist.

An interesting connection has thus emerged between the LT transition and MDR. Although MDR is typically studied at much higher Re, it should be stressed that experimental observation of MDR in the LT transition regime dates back to the time of its initial discovery [2]. Recently, Samanta *et al.* [39] experimentally explored the LT transition regime in pipe flow of dilute polymer solutions. Both early and delayed turbulence were observed in the study. Delayed turbulence occurs at lower polymer concentration and is qualitatively similar to the Newtonian LT transition. For higher polymer concentration, early turbulence kicks in, which appears to be a new type of instability driven by both elasticity and inertia. This study reconciled the seemingly conflicting phenomena of delayed and early transition and offered a consistent explanation for the coexistence of two parallel transition mechanisms. In addition, for at least one parameter set, the flow rate of this instability follows the MDR asymptote, suggesting a potential link between this so-called elastoinertial turbulence (EIT) and MDR. Direct numerical simulation of EIT showed different vortex structures than the regular inertia-driven turbulence [40].

Whether MDR is dominated solely by weak Newtonian turbulent states or it becomes overtaken by EIT at high levels of elasticity (as suggested by Dubief *et al.* [40]) is still a subject for further investigation. However, these advances in the past five years do point toward one consensus, that the LT transition is a region connecting all important unsolved problems in viscoelastic turbulence, including the transition, DR onset, and MDR. At the center of this region is the ES. Hitherto, Xi and Graham [38] remains the only reported study of viscoelastic ES. In addition to its major observation that ES mean flow is insensitive to polymer effects, mean velocity profiles obtained in that study were strikingly close to the Virk [2] logarithmic law. However, solutions were found for only one computational domain: System-size effects still need to be investigated for a definitive answer. It is also unclear how the ES fits in the recent framework that explains the convergence to MDR based on the dynamical transition between active and hibernating states [4,26,29]. The current study aims to address these issues. On the other hand, compared with the large volume of recent research on Newtonian ESs [35,36,41–48], the current study will offer a fresh perspective of direct relevance to DR research. Particular focus will be on flow statistics and polymer-flow interaction at the ES.

II. METHODOLOGY

A. Formulation and simulation details

We consider flow driven by a constant mean pressure gradient in the plane Poiseuille geometry. The x, y, and z coordinates are aligned with the streamwise, wall-normal, and spanwise directions, respectively. The no-slip boundary condition is applied at both walls and periodic boundary conditions are adopted in the x and z directions. The half height of the channel l is chosen as the characteristic length scale and the Newtonian laminar centerline velocity U at the same pressure drop is the velocity scale. The nondimensional size of the simulation box is denoted by $L_x \times 2 \times L_z$.

The conservation equations of momentum and mass are

$$\frac{\partial \boldsymbol{v}}{\partial t} + \boldsymbol{v}\cdot\nabla\boldsymbol{v} = -\nabla p + \frac{\beta}{\mathrm{Re}}\nabla^2\boldsymbol{v} + \frac{2(1-\beta)}{\mathrm{Re\,Wi}}(\nabla\cdot\boldsymbol{\tau}_p), \tag{2}$$

$$\nabla\cdot\boldsymbol{v} = 0, \tag{3}$$

in which all variables are nondimensionalized with the turbulent outer scales: velocity by U, distance by l, time by l/U, and pressure by ρU^2. Correspondingly, the Reynolds number is $\mathrm{Re} \equiv \rho U l/\eta$. Here ρ is the total density of the fluid; $\eta \equiv \eta_s + \eta_p$ is the total zero-shear-rate viscosity, where s and p denote the solvent (i.e., the Newtonian fluid) and polymer contributions, respectively. The Weissenberg number $\mathrm{Wi} \equiv 2\lambda U/l$ is defined as the product of the polymer relaxation time λ and the Newtonian mean wall shear rate. (With the constraint on the mean pressure gradient, it can be shown from a total force balance that the mean wall shear rate is constant for Newtonian flows $-dU_m/dy = 2U/l$; for dilute polymer solutions, shear thinning is negligible and $dU_m/dy \approx 2U/l$.) The viscosity ratio $\beta \equiv \eta_s/\eta$ depends on the polymer concentration c_p: In dilute solutions, $1-\beta \propto c_p$.

Near-wall turbulent structures and statistics are often measured in turbulent inner scales [19], where stresses are scaled with the mean wall shear stress τ_w (averaged over time and the wall surface area as well as between the two walls), velocities by the friction velocity $u_\tau \equiv \sqrt{\tau_w/\rho}$, and lengths by the viscous length scale or wall unit $\delta_v \equiv \eta/\rho u_\tau$. Quantities nondimensionalized with these scales are marked with a superscript $+$, e.g., $v_x^+ \equiv v_x/u_\tau$. Because of the constant mean wall shear rate, τ_w is constant and so are the friction

Reynolds number $\mathrm{Re}_\tau \equiv \rho u_\tau l/\eta = \sqrt{2\,\mathrm{Re}}$ and eddy turnover time $l/u_\tau = \sqrt{\mathrm{Re}/2}$. Meanwhile, many quantities we report are instantaneous (i.e., defined at a given time instant) and describe events near one wall only. It is thus more relevant to use the instantaneous wall shear stress τ_w^* (averaged over the surface of the nearer wall for a given time) to calculate the inner scales. The corresponding nondimensionalized variables will be marked with a superscript $*$. The wall-normal coordinate in inner scales, i.e., y^+ and y^*, has its origin defined at the wall, as per convention.

The last term on the right-hand side of Eq. (2) contains the polymer stress tensor $\boldsymbol{\tau}_p$, obtained from the finitely extensible nonlinear elastic – Peterlin approximation (FENE-P) constitutive equation [49]

$$\frac{\boldsymbol{\alpha}}{1-\frac{\mathrm{tr}(\boldsymbol{\alpha})}{b}} + \frac{\mathrm{Wi}}{2}\left(\frac{\partial\boldsymbol{\alpha}}{\partial t} + \boldsymbol{v}\cdot\nabla\boldsymbol{\alpha} - \boldsymbol{\alpha}\cdot\nabla\boldsymbol{v} - (\boldsymbol{\alpha}\cdot\nabla\boldsymbol{v})^{\mathrm{T}}\right) = \left(\frac{b}{b+2}\right)\boldsymbol{\delta}, \tag{4}$$

$$\boldsymbol{\tau}_p = \frac{b+5}{b}\left[\frac{\boldsymbol{\alpha}}{1-\frac{\mathrm{tr}(\boldsymbol{\alpha})}{b}} - \left(\frac{b}{b+2}\right)\boldsymbol{\delta}\right]. \tag{5}$$

Here $\boldsymbol{\delta}$ is the Kronecker delta tensor. In the FENE-P, polymer molecules are described with a dumbbell model: two beads connected by a finitely extensible nonlinear elastic spring. Extension and orientation of a polymer chain is measured by its end-to-end vector $\boldsymbol{Q}$ and the conformation tensor $\boldsymbol{\alpha} \equiv \langle \boldsymbol{Q}\boldsymbol{Q}\rangle$ ($\langle\cdot\rangle$ denotes ensemble average). The trace of the $\boldsymbol{\alpha}$ tensor measures the polymer chain extension, whose upper limit is determined by the b parameter: $\max[\mathrm{tr}(\boldsymbol{\alpha})] < b$.

A total of four nondimensional parameters specify the entire system: Re, Wi, β, and b. Three different Re, 3600 ($\mathrm{Re}_\tau = 84.85$), 7200 ($\mathrm{Re}_\tau = 120$), and 14 400 ($\mathrm{Re}_\tau = 169.71$), are studied here for Newtonian flow, but only $\mathrm{Re} = 3600$ is studied for viscoelastic cases, due to the high computational cost of edge tracking (see Sec. II B). (The LT transition occurs at $\mathrm{Re}_{\mathrm{crit}} \approx 1000$ in plane Poiseuille flow [50].) The importance of β and b becomes apparent in considering the nondimensional extensibility parameter $\mathcal{E}$, defined as the polymer contribution to the steady-state stress in uniaxial extensional flow at the high Wi limit. For the FENE-P,

$$\mathcal{E} = \frac{2b(1-\beta)}{3\beta}. \tag{6}$$

For a dilute solution ($1-\beta \ll 1$), significant effects of polymer on turbulence are only expected when $\mathcal{E} \gg 1$. Viscoelastic simulations reported in this study are all performed with $\beta = 0.97$ and $b = 5000$, corresponding to $\mathcal{E} = 103.09$.

Equations (2)–(5) are coupled and numerically integrated in time with a third-order semi-implicit backward-differentiation–Adams-Bashforth scheme [51]. Fourier-Chebyshev-Fourier spatial discretization is applied in all variables and nonlinear terms are calculated with the collocation method. The numerical grid spacings for the periodic directions are $\delta_x^+ = 8.57$ and $\delta_z^+ = 5.11$ or 5.19 (depending on L_z^+). The number of Chebyshev modes used in the y direction increases with Re, $N_y = 73$ for $\mathrm{Re} = 3600$, 101 for $\mathrm{Re} = 7200$, and 145 for $\mathrm{Re} = 14\,400$, to keep the range of δ_y^+ roughly the same. For $\mathrm{Re} = 3600$, at which most data will be reported, $N_y = 73$ gives $\delta_{y,\min}^+ = 0.081$ at the walls and $\delta_{y,\max}^+ = 3.7$ at the channel center. The time step size is chosen considering the Courant-Friedrichs-Lewy stability condition and also varies with Re: $\delta_t = 0.02$ for $\mathrm{Re} = 3600$, $\delta_t = 0.0125$ for $\mathrm{Re} = 7200$, and $\delta_t = 0.01$ for $\mathrm{Re} = 14\,400$. An artificial diffusion term $1/(\mathrm{Sc\,Re})\nabla^2\boldsymbol{\alpha}$ with $\mathrm{Sc} = 0.5$ is added to the FENE-P equation to improve its numerical stability. Usage of artificial diffusivity and its effects on simulation results are well studied in the literature [52]. Our choice of diffusivity magnitude is no larger than most other DNS studies and should not affect the physical interpretation of the results [10,22,23,53,54]. The numerical procedure we use is the same as a number of previous studies; see, e.g., [24,55], where more details can be found. The DNS code used in this study is custom developed based on CHANNELFLOW, a C++ library for Newtonian DNS [56].

B. Numerical edge tracking

Edge-state solutions can be numerically computed using a standard DNS code. The method has been well established in Newtonian ES studies and can be straightforwardly extended to viscoelastic cases. Here we briefly recapitulate the essence of the method; interested readers are referred to the works of Skufca *et al.* [34], Schneider *et al.* [44], and Duguet *et al.* [45] for details.

Given a pair of initial states $\boldsymbol{X}_T = [\boldsymbol{v}_T, \boldsymbol{\alpha}_T]$ and $\boldsymbol{X}_L = [\boldsymbol{v}_L, \boldsymbol{\alpha}_L]$ known to bound the turbulent basin and laminar state, respectively, a straight line connecting them in the state space

$$\boldsymbol{X}_\omega \equiv \omega\boldsymbol{X}_T + (1-\omega)\boldsymbol{X}_L \tag{7}$$

must intersect with the LT boundary at least once, say, at $\omega = \omega_e$. Numerical approximations to the intersection can be found through repeated bisections and DNS shooting tests. A pair of such states is denoted by $\boldsymbol{X}_{\omega_e^+}$ and $\boldsymbol{X}_{\omega_e^-}$: ω_e^+ (ω_e^-) is infinitesimally larger (smaller) than ω_e. Dynamical (DNS) trajectories initiated therefrom, $\boldsymbol{X}_{\omega_e^+}(t)$ and $\boldsymbol{X}_{\omega_e^-}(t)$, will travel along the edge for a while before diverging to opposite destinations, effectively pinching and numerically approximating an edge trajectory for a time period. A new round of repeated bisections and shootings are started at the diverging point to further extend the numerical edge solution.

In this study, bisections are carried out to a numerical precision of $\omega_e^+ - \omega_e^- = 10^{-8}$. A new round is initiated when the difference in the turbulent kinetic energy (TKE) k_b between the pinching trajectories grows into the range of 10^{-6}–10^{-5}, where

$$k \equiv \tfrac{1}{2}\left(v_x'^2 + v_y'^2 + v_z'^2\right). \tag{8}$$

(Hereinafter, a prime denotes the fluctuating component, e.g., $v_x' \equiv v_x - \langle v_x\rangle$, and the subscript b indicates quantities averaged over the bulk, i.e., over the x, y, and z directions.) Time series of k_b from a typical edge-tracking process are shown in Fig. 1. From an arbitrarily chosen pair of initial states, the k_b value becomes statistically converged after about 2000 time units (TUs), indicating that the asymptotic ES has been reached. Different initial state pairs have also been tested and the same converged state is found.

The simulation box used in Fig. 1, $L_x^+ \times L_z^+ = 360 \times 140$, is a typical size of a so-called minimal flow unit (MFU) [55,57],

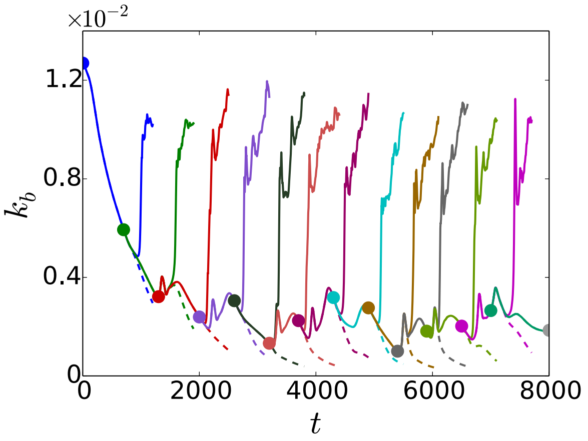

FIG. 1. Time series of bulk-averaged TKE of DNS shooting trajectories pinching an edge solution (Newtonian, with $L_x^+ \times L_z^+ = 360 \times 140$). Different colors are used for different rounds of shooting. Shooting start points are shown with circles. Solid lines denote $\boldsymbol{X}_{\omega_e^+}(t)$ and dashed lines $\boldsymbol{X}_{\omega_e^-}(t)$.

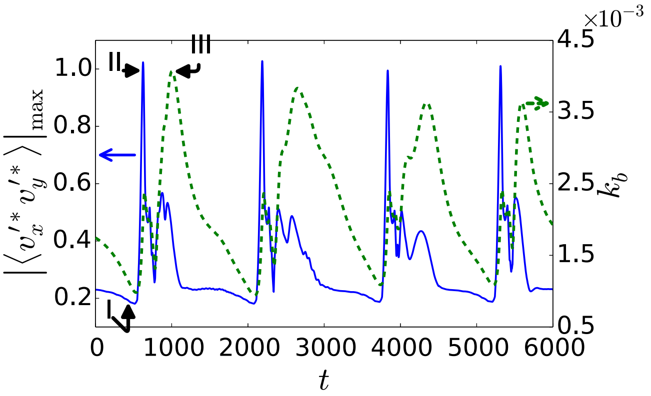

FIG. 2. The ES time series for Wi = 28 and $L_x^+ \times L_z^+ = 720 \times 140$: the blue solid line (left axis) shows the peak value of the instantaneous RSS profile and the green dashed line (right axis) shows the TKE (bulk average).

the smallest periodic domain that sustains turbulence, for Newtonian channel flow. Results reported below are however all from longer boxes with $L_x^+ = 720$, because viscoelastic turbulence typically features elongated flow structures and longer streamwise correlations [20–24,30]. Two spanwise domain sizes $L_z^+ = 140$ and 230 are studied ($L_z^+ = 140$ was used in [38]). All our qualitative conclusions, such as structural features of ESs, flow-polymer interactions, and implications on DR, are consistent between different box sizes, although quantitative results do vary (discussed below). The narrower (720×140) box does not support sustained turbulent solutions at high Wi (e.g., the minimal L_z^+ for sustained turbulence at Wi = 28 is 230 [30,55]), meaning that the turbulent attractor is now replaced by a transient saddle or repeller [58] and the edge becomes a weak basin boundary [59]. In this case and for edge-tracking purposes, a shooting trajectory is identified as turbulence bound if there is at least one strong burst in k_b (one order of magnitude higher than typical ES values) before its decay toward the laminar state.

III. RESULTS

A. Overview

Our discussion henceforth focuses only on the asymptotic ES, the statistically converged part of an edge solution. Figure 2 shows the time series of a typical viscoelastic ES (the Newtonian case is similar [38]). In contrast to regular DNS trajectories, which show chaotic fluctuations (see Fig. 3), the ES is dominated by nearly periodic dynamical patterns. The blue line shows the peak magnitude of the instantaneous Reynolds shear stress (RSS) profile $-\langle v_x'^* v_y'^* \rangle$ ($*$ indicates quantities in instantaneous inner scales (see II A), $\langle\cdot\rangle$ indicates average over x and z, and the absolute value $|\cdot|$ is taken because $-\langle v_x'^* v_y'^* \rangle$ changes sign across the channel centerline [see Fig. 7(b)]). We arbitrarily define a period to start at a minimum in $|v_x'^* v_y'^*|_{\max}$ (instant I), i.e., when near-wall turbulent activity is lowest. A rapid shoot up of $|v_x'^* v_y'^*|_{\max}$ then quickly leads to a peak at instant II. The rise of k_b comes after the RSS and the maximum is reached at instant III. This short burst of higher turbulent activities around instants II and III is followed by a longer quiescent period when k_b slowly decays to its minimum.

Note that, despite our use of the word burst, the Reynolds stress magnitude, both $|v_x'^* v_y'^*|_{\max}$ and k_b, of the ES during these periods is still much lower than regular turbulence. For example, in the 720×230 box (Fig. 3), $|v_x'^* v_y'^*|_{\max}$ of the ES is on average 2–3 times lower than a regular DNS trajectory. The difference is even larger when bulk averages (instead of profile peaks) are compared, e.g., k_b of the ES is about 5–6 times lower than that of a regular DNS (Fig. 4). Comparing the time series in Fig. 3, not only are fluctuations at the ES more regular (quasiperiodic), their time scale is also much longer than a regular DNS and reaches $O(1000)$ TUs. Newtonian ES solutions are very similar to the viscoelastic ones and thus are not shown here. Periodic dynamics has also been commonly observed in previous studies of plane Poiseuille ESs [42,48]. Interestingly, in the shorter 360×140 box (Fig. 1), the fluctuations are not periodic but are still smoother and less chaotic than a regular DNS. Alternation

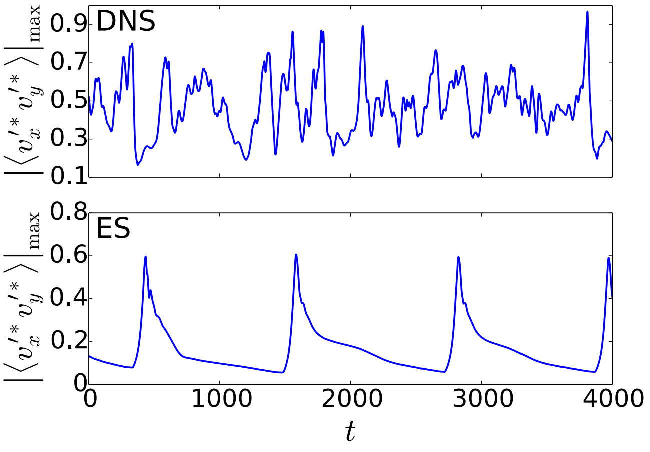

FIG. 3. Time series of the peak value of the instantaneous RSS profile: comparison between regular DNS (top) and the ES (bottom) (both with Wi = 28 and $L_x^+ \times L_z^+ = 720 \times 230$).

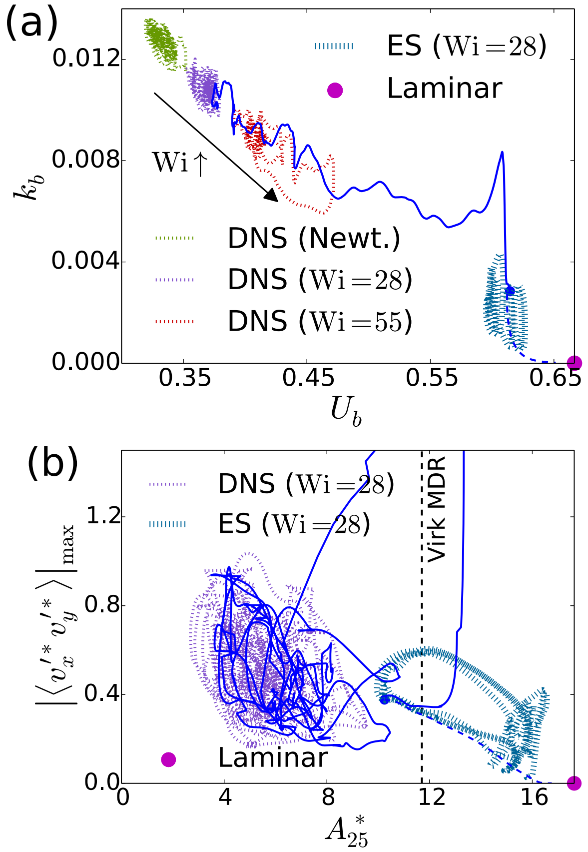

FIG. 4. State-space projections of regular DNS trajectories and the ES with $L_x^+ \times L_z^+ = 720 \times 650$ for Wi = 55 DNS, as per [30], and 720 × 230 for the rest. Two diverging DNS trajectories from the ES are shown in thin blue (solid and dashed) lines.

between periodic and aperiodic dynamics was also reported in Newtonian plane Poiseuille flow with varying Re [48].

State-space trajectories of different solution objects are projected onto the k_b-U_b (bulk average of v_x) plane in Fig. 4(a). Newtonian turbulence has the highest friction drag and the corresponding DNS solution cloud sits at the upper left corner. Solution clouds for viscoelastic DNS move toward the direction of higher U_b and lower k_b as Wi increases. The ES has significantly lower friction drag and is found farther to the lower right. With an infinitesimal perturbation, the ES can either (thin blue solid) grow into full turbulence or (thin blue dashed) decay to the laminar state ($U_b = 2/3$ and $k_b = 0$).

Recall the logarithmic law relationship in Eq. (1); an analogous formulation can be written for the instantaneous mean velocity profile $U_m^*(y^*)$. It was previously found that the logarithmic law slope A^* from the DNS of the MFU instantly reflects the activities of near-wall coherent structures and the correlation is strongest within the layer of $20 \lesssim y^* \lesssim 30$ [26]. To calculate this slope, we obtain from the logarithmic law that

$$A^* = y^* \frac{dU_m^*}{dy^*}; \tag{9}$$

DNS and ES solutions shown in Fig. 4(a) are then reprojected to the $|v_x'^* v_y'^*|_{\max}$-A^*_{25} (A^*_{25} being the A^* value at $y^* = 25$) plane in Fig. 4(b). In this projection, the turbulence-bound dynamical trajectory initiated from the ES (thin blue solid line) quickly converges to the same region as the steady-state DNS, after a strong initial burst in RSS. (Note that steady-state DNS solutions for Newtonian and Wi = 55 cases are omitted for clarity: Both solution clouds overlap heavily with the Wi = 28 cloud; the Newtonian one shifts slightly to the upper left and Wi = 55 to the lower right.) The converged part densely samples the core of the steady-state cloud, corresponding to active turbulence, and hibernating turbulence appears as occasional excursions toward the ES. The ES fluctuates near the laminar state most of the time, but during its bursting phase (peaks in Fig. 3) it extends toward the upper left and overlaps the hibernating region. Interestingly, A^*_{25} of this junction is very close to $A^+_{\mathrm{Virk}} = 11.7$. This suggests that one or more of the traveling-wave solutions forming the ES [33,36] are also governing the dynamics of turbulence hibernation, a promising lead for pinpointing the origin of MDR. These coordinates A^*_{25} and $|v_x'^* v_y'^*|_{\max}$ directly measure the activities of near-wall coherent structures, from which the active-hibernating transition and hibernation-ES connection are more readily revealed. These dynamical features are less sensitive to domain-wide averages, such as k_b and U_b used in Fig. 4(a). For instance, when a coherent structure enters the hibernating phase, the local velocity gradient, measured by A^*, quickly shoots up [26]; it will, however, take $O(\mathrm{Re})$ TUs for this effect to be felt across the channel. By comparison, at Wi = 28 the typical duration of hibernating periods is only ∼200 TUs [26,29], which explains why such transitions are not reflected in U_b. In Fig. 4(a), hibernating turbulence only becomes visible at much higher Wi (=55).

Structural evolution is best observed in the spatiotemporal distribution of wall shear rate $\partial v_x/\partial y|_w$ shown in Fig. 5. The image of the 720 × 140 box [Fig. 5(a)] starts in a quiescent period when a single low-shear streak is observed. The burst occurs at $t \approx 600$ as this streak suddenly turns into a high-shear one, with another high-shear streak emerging next to it. Both streaks are strong in terms of the $\partial v_x/\partial y|_w$ magnitude and coexist for a short period of time. The average of $\partial v_x/\partial y|_w$ over the wall also sharply increases during the burst, indicating strong near-wall turbulent activities. At $t \approx 1000$ (around instant III in Fig. 2), the high-shear streak at $z^+ \approx 50$ becomes wider in size and remains strong in magnitude until $t \approx 1200$. Meanwhile, the one at $z^+ \approx 120$ quickly decays. Behind it two low-shear streaks merge into one, which dominates the domain for the next quiescent period. This new low-shear streak is shifted for about half L_z^+ compared with the old one. Alternation between single-streak and double-streak structures, as well as the shift of streak location between periods, was also reported for plane Poiseuille Newtonian ESs in near-minimal channels [42].

The bursting-quiescent periodic dynamics is qualitatively similar in the wider box (720 × 230 [Fig. 5(b)]). The quiescent period is still dominated by one strong low-shear streak, which is sometimes accompanied by another significantly weaker low-shear streak (e.g., for $t \lesssim 400$). At the beginning of the bursting period ($t \approx 400$) the dominant low-shear streak again turns into a high-speed one, which is strong but short-lived. Low-shear streaks on its flanks converge at $z^+ \approx 100$, forming the dominant pattern for the next quiescent period. In comparison, dynamics of regular DNS [Fig. 5(c)] in

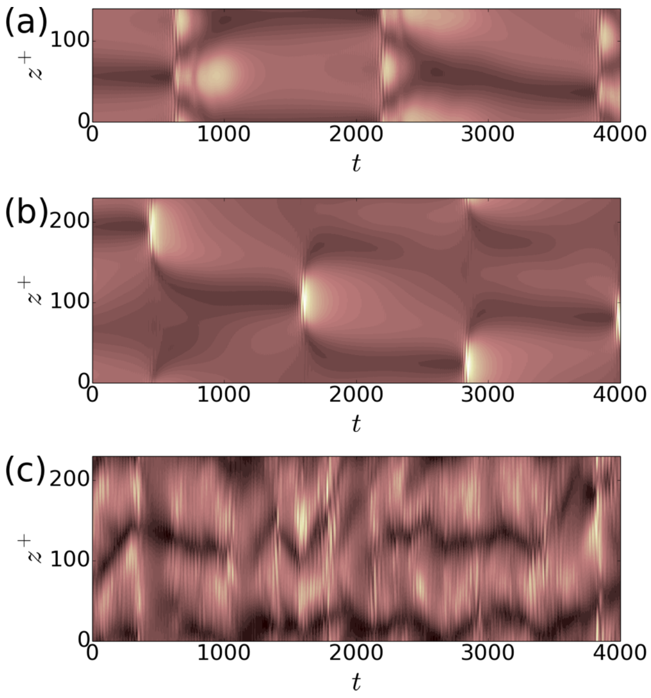

FIG. 5. Spatiotemporal wall shear rate evolution (Wi = 28) for (a) the ES with $L_x^+ \times L_z^+ = 720 \times 140$, (b) the ES with 720×230, and (c) DNS with 720×230. The distribution of $\partial v_x/\partial y|_w$ is measured along the $x = 0$ line and is plotted in z^+-t coordinates. The same color scale, from 1 (dark) to 6 (bright), is used for all panels. The time axes are consistent with those in Figs. 2 and 3.

the same box size is almost always dominated by two low-shear streaks, giving an average streak spacing of ≈115 (close to the experimental measurement of ≈100 [60]). Unlike the ES, where the streaks sit at the same position for extended periods with sudden shifts occurring with the bursts, streaks in regular DNS constantly drift in the z direction. Rapid oscillations in color shades along the t axis reflect strong and fast fluctuations in regular turbulent dynamics, whereas at the ES color changes are smooth except for the bursts.

B. Flow statistics and DR

Flow statistics of ES received little previous attention even for the well-studied Newtonian case, but are central to our interest in DR. The most important statistic in this regard is the mean velocity: $U_m^+(y^+)$ profiles of Newtonian and viscoelastic (Wi = 28) ESs are plotted in Fig. 6 for different box sizes. Reference lines are given for the viscous sublayer [19]

$$U_m^+ = y^+ \tag{10}$$

as well as the PvK (for Newtonian turbulence) and Virk (for MDR) logarithmic laws [see Eq. (1)]. For both box sizes, Newtonian and viscoelastic profiles overlap one another. The collapsed profiles of the 720×140 box are strikingly close to the Virk MDR, whereas those of the 720×230 box lie slightly above. For the 720×140 box, several other Wi were also tested previously and the $U_m^+(y^+)$ profile showed no Wi dependence [38]. This study further demonstrates that the insensitivity of mean flow to polymer effects is a general observation irrespective of the domain size. The magnitude of U_m^+ does vary with the domain size however. This can be understood by comparing the patterns in Figs. 5(a) and 5(b): In the wider box the streak dynamics is mostly localized in a limited z range, whereas in the narrower box the domain is almost filled entirely. This finding is consistent with previous Newtonian ES studies [36,48]. Since a localized turbulent spot is surrounded by near-laminar flow regions [61,62], the xz-area average of v_x depends on the relative proportions of the two flow patterns and thus must vary with the domain size. Nevertheless, our ES study offers clear explanations for both the existence and universality of MDR. With the most marginal form of turbulence not yielding under the influence of polymers, polymer-induced DR has to be bounded by an upper limit and the limit must be the same for different polymer solutions. It also explains why complete laminarization is not observed in experiments. Meanwhile, with the ES mean velocity dependent on the domain size, the quantitative origin of the Virk asymptote remains elusive. The ES is likely only one of many flow states invariant under polymer effects: How their collective dynamics results in the Virk logarithmic law is a subject for future investigation.

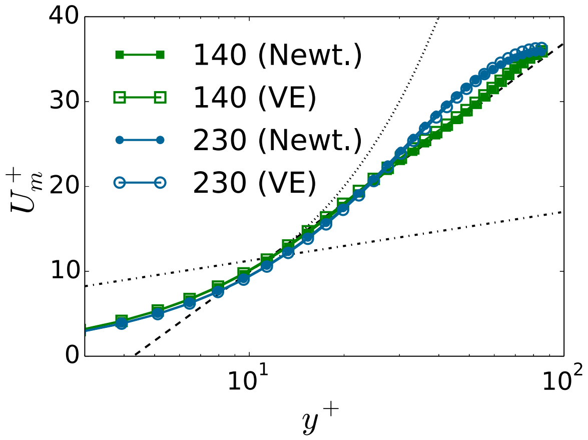

FIG. 6. Mean velocity profiles of Newtonian (Newt.) and viscoelastic (VE) (Wi = 28) ESs for $L_x^+ \times L_z^+ = 720 \times 140$ (140) and 720×230 (230). The viscous sublayer is denoted by ...., the PvK logarithmic law by -.-.-., and the Virk MDR by - - - -.)

In Fig. 7(a) we break down the time average and present the mean velocity at different ES instants. The profile of instant I, taken at the end of a quiescent period, is only slightly higher than the time average. At instants II and III, i.e, within the bursting period, the profiles are lower and crooked. The profile slopes are markedly suppressed between $y^* \approx 20$ and 40, a sign of significant turbulent activities localized in that layer.

Structural localization in the y direction is more obvious in the RSS profiles $-\langle v_x'^+ v_y'^+ \rangle$ [Fig. 7(b)]. For regular DNS trajectories, both Newtonian and viscoelastic, the profiles are antisymmetric across the center plane $y = 0$. (The sign changes because at $y < 0$ positive v_y points away from the bottom wall, whereas at $y > 0$ it points toward the top wall.) The total shear stress

$$\langle \tau_{xy}^+ \rangle = \beta dU_m^+/dy^+ + \langle -v_x'^+ v_y'^+ \rangle + \frac{1-\beta}{\mathrm{Wi}} \langle \tau_{p,xy} \rangle \tag{11}$$

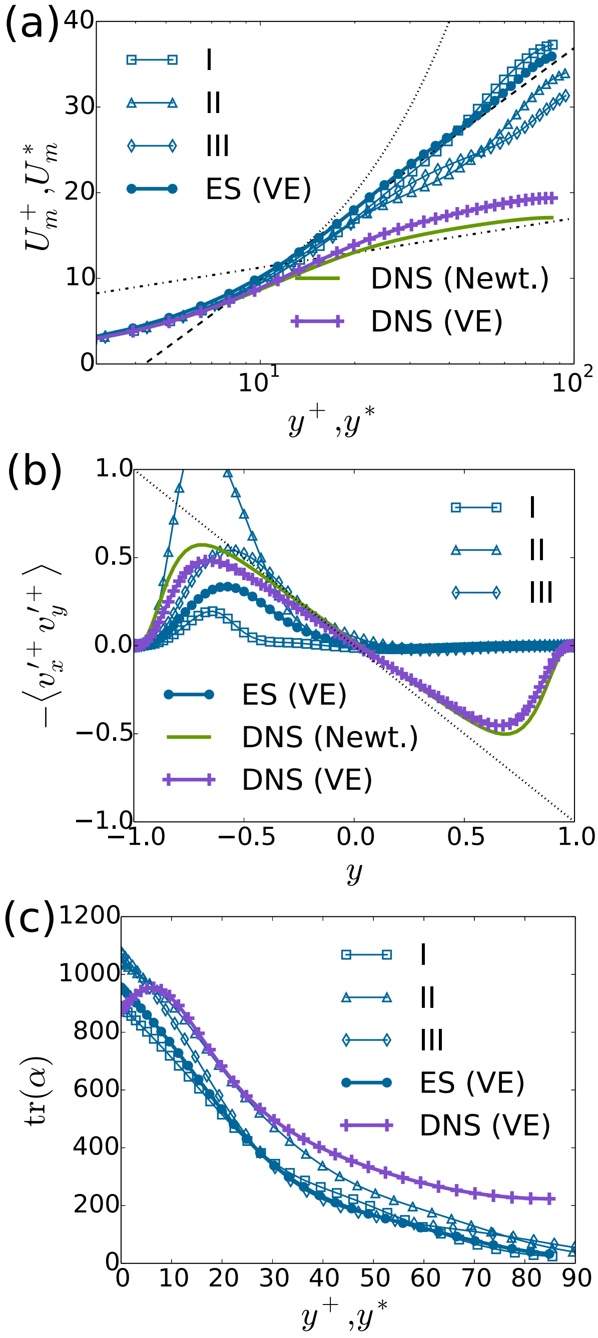

FIG. 7. Flow and polymer conformation statistics for (a) mean velocity (viscous sublayer, ...; PvK logarithmic law, -.-.-.; and Virk MDR, - - - -), (b) Reynolds shear stress [dashed line shows total shear stress (12)], and (c) tr($\boldsymbol{\alpha}$). Profiles include the time average of the Wi = 28 ES ($L_x^+ \times L_z^+ = 720 \times 140$), marked with ES (VE), and its selected instants (indicated in Fig. 2), as well as time averages of the Newtonian (Newt.) and Wi = 28 (VE) DNS ($L_x^+ \times L_z^+ = 720 \times 230$). In (a) and (c), + units are used for time-average profiles and $*$ units for instantaneous ones; in (b) + units are used for all profiles.

contains components of [in the order given on the right-hand side of Eq. (11)] mean viscous shear stress, RSS, and polymer shear stress [54,63]. Its magnitude, derived from the steady-state shear stress balance [19], is

$$\langle \tau_{xy}^+ \rangle = 1 - y \tag{12}$$

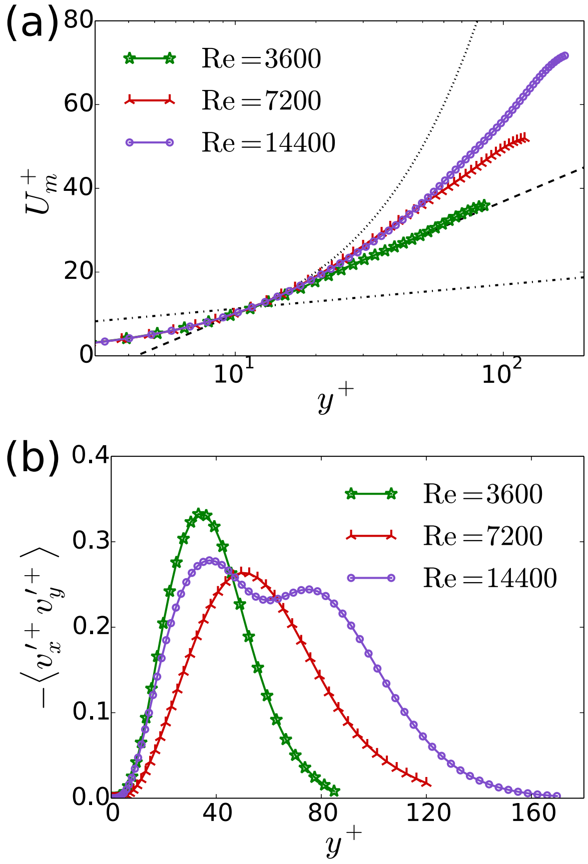

FIG. 8. Newtonian ES flow statistics at different Re ($L_x^+ \times L_z^+ = 720 \times 140$) for the (a) mean velocity (viscous sublayer, ...; PvK logarithmic law, -.-.-.; and Virk MDR, - - - -) and (b) RSS.

[dashed line in Fig. 7(b)]. Viscous shear stress is large only in the region closest to the walls, beyond which $\langle \tau_{xy}^+ \rangle$ is dominated by $-\langle v_x'^+ v_y'^+ \rangle$ [19]. The $-\langle v_x'^+ v_y'^+ \rangle$ profile of viscoelastic DNS is lower than the Newtonian one because of the rise of polymer stress [54,63–65].

For the ES, however, the RSS distribution is highly skewed: Large magnitude and strong fluctuations are only observed at one side of the channel. The RSS measures the momentum transfer from mean flow to fluctuating velocities through near-wall coherent structures. Strong asymmetry in these profiles indicates that turbulent activities at the ES are only significant near one of the walls, whereas the rest of the channel is occupied by near-laminar flow patterns. Localization is also found in Newtonian ESs [42,48] and is physically plausible: It only takes a localized disturbance to trigger turbulence from a laminar base flow [66,67]. Because of this asymmetry, when plotting ES results we always choose the side with significant turbulent activities wherever applicable [Figs. 4(b), 5(a), 5(b), 6, 7(a), 7(c), 8, 11, and 12].

As the bursting phase starts (I → II), $-\langle v_x'^* v_y'^* \rangle$ rapidly shoots up: The spike magnitude of instant II is more than double that of regular DNS. From II to III, RSS quickly decays while k_b increases (see Fig. 2). Vanishing RSS was often cited as a feature of MDR as well as the hypothetical marginal turbulent state [27,28,64]. It is clear now that even for the ES in its quiescent phase, $-\langle v_x'^* v_y'^* \rangle$ never drops to zero. The distinction of RSS at the ES, compared with regular DNS, is, however, its localization. This suggests that the real indicator of MDR is likely the spatial distribution of RSS rather than its magnitude. Indeed, a localized RSS distribution (in y) has been consistently observed at high levels of DR (HDR) and MDR, as well as in hibernating turbulence [23,26,54,55,68].

Polymer extension in the flow field is measured by tr($\boldsymbol{\alpha}$) and plotted in Fig. 7(c). Interestingly, despite its lower overall turbulent activities, the tr($\boldsymbol{\alpha}$) magnitude of the ES is comparable with that of regular DNS. It also does not vary much between quiescent and bursting phases when instantaneous profiles are compared. The most notable difference is in the curve shape: The DNS profile has a maximum at $5 \lesssim y^+ \lesssim 10$, whereas all ES profiles monotonically decrease with y^+ (or y^*). To understand this, note first that even without turbulent fluctuations, the mean velocity $U_m(y)$ can still provide sufficient shear motion to stretch polymer chains. This effect is strongest at the walls where $dU_m(y)/dy$ is highest and decreases monotonically with increasing y^+ (y^*). The mean shear aligns polymers in the x direction, whose contribution will all go to the α_{xx} component. Turbulent activities, on the other hand, deform polymer chains through strong but transient local extensional motions, which can occur in any direction. This contribution is zero at the walls and highest where coherent structures are most active, i.e., the buffer layer $5 \lesssim y^+ \lesssim 30$ [19,69]. Monotonic profiles observed at the ES indicate that its flow field is dominated by the mean shear. Indeed, at the ES as well as in hibernating turbulence, α_{yy} and α_{zz} are orders of magnitude lower than both α_{xx} and their respective magnitudes in active turbulence [26,38]. An off-wall peak in tr($\boldsymbol{\alpha}$) can only come from strong polymer-turbulence interaction and in DNS it is typically observed at HDR [55].

Figure 8 shows the Re dependence of the Newtonian ES in the 720 × 140 box. With increasing Re, the $U_m^+(y^+)$ profile [Fig. 8(a)] deviates from the Virk logarithmic law and rises to higher magnitude. This of course is not in accord with the scaling behavior of MDR, which has the same $U_m^+(y^+)$ logarithmic law for different Re [2]. It again can be explained by the spatial localization of the ES dynamics and is yet another indication that although the ES, with its invariance against polymer effects, explains the existence and universality of MDR, the quantitative magnitude of Virk logarithmic law remains unsolved. Localization of the $-\langle v_x'^* v_y'^* \rangle$ magnitude [Fig. 8(b)] is observed at all Re studied and all profiles have a primary peak at $35 \lesssim y^+ \lesssim 45$. Interestingly, for the highest Re = 14 400, a secondary peak shows up at $y^+ \approx 80$, whose origin is as yet unclear. At least for a normal component of Reynolds stress, the emergence of a secondary peak as Re increases is a feature recently found in experiments [70].

C. Flow structures and interaction with polymers

It is now increasingly evident that the ES and hibernating turbulence are intrinsically connected. Similarities between the two are also observed in flow structures and their interaction with polymers.

Near-wall turbulent activities are dominated by vortices and velocity streaks [71–74]. Vortices in a flow field can be identified using the Q criterion [75,76], in which vortex strength is measured with

$$Q \equiv \tfrac{1}{2}(\|\boldsymbol{\Omega}\|^2 - \|\boldsymbol{\Gamma}\|^2), \tag{13}$$

with $\boldsymbol{\Omega}$ being the vorticity tensor

$$\boldsymbol{\Omega} \equiv \tfrac{1}{2}(\nabla \boldsymbol{v} - \nabla \boldsymbol{v}^T), \tag{14}$$

$\boldsymbol{\Gamma}$ being the rate of strain tensor

$$\boldsymbol{\Gamma} \equiv \tfrac{1}{2}(\nabla \boldsymbol{v} + \nabla \boldsymbol{v}^T), \tag{15}$$

and $\|\cdot\|$ representing the Frobenius tensor norm. A positive Q value indicates stronger local rotation than deformation and an isosurface there gives direct visualization of vortex configuration. In Figs. 9 and 10 Q isosurfaces are shown along with those of tr($\boldsymbol{\alpha}$) and $\alpha_{yy} + \alpha_{zz}$. Isosurface levels are different for each image and are chosen according to the maximum and minimum values found in each domain: $Q_{\text{iso}} = 0.25 Q_{\max}$, $\text{tr}(\boldsymbol{\alpha})_{\text{iso}} = 0.5[\text{tr}(\boldsymbol{\alpha})_{\max} + \text{tr}(\boldsymbol{\alpha})_{\min}]$, and $(\alpha_{yy} + \alpha_{zz})_{\text{iso}} = 0.5[(\alpha_{yy} + \alpha_{zz})_{\max} + (\alpha_{yy} + \alpha_{zz})_{\min}]$.

For the ES (Fig. 9), all activities are concentrated at one side of the channel owing to the spatial localization. At the end of the quiescent period (instant I), the vortices are elongated and extend across the whole domain. With the burst of RSS (instant II), vortices move much closer to the wall and their spacing is substantially reduced. The following drop of RSS and rise of k_b (instant III) come as vortices lift up to the bulk region. The Q_{iso} magnitude at instant II is one order of magnitude higher than that of the other two, which reaffirms the burst of RSS as the primary moment of turbulent activity. Note that in all instants, tr($\boldsymbol{\alpha}$) isosurfaces do not conform to the shape and position of vortices and lie as flat sheets near the walls, where the mean shear is strongest. Meanwhile, isosurfaces of the transversal components $\alpha_{yy} + \alpha_{zz}$ always accompany the vortices. This is consistent with the discussion in Sec. III B that yy and zz components offer a more reliable depiction of the polymer-turbulence interaction. Note also the small magnitudes of α_{yy} and α_{zz}: Even at instant II, they are only slightly higher than the equilibrium (unstretched) value of

$$\alpha_{xx,\text{eq}} = \alpha_{yy,\text{eq}} = \alpha_{zz,\text{eq}} = \frac{b}{b+5} \approx 1. \tag{16}$$

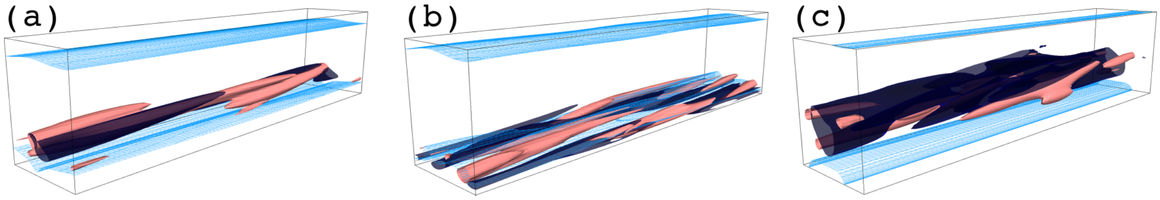

FIG. 9. Isosurfaces of Q (pink solid), tr($\boldsymbol{\alpha}$) (light blue meshed), and $\alpha_{yy} + \alpha_{zz}$ (dark blue translucent) for the three selected instants indicated in Fig. 2; the isosurface levels $[Q_{\text{iso}}, \text{tr}(\boldsymbol{\alpha})_{\text{iso}}, (\alpha_{yy} + \alpha_{zz})_{\text{iso}}]$ used in each instant are different: (a) I $[1.68 \times 10^{-3}, 529.61, 2.99]$, (b) II $[1.12 \times 10^{-2}, 670.98, 10.52]$, and (c) III $[6.00 \times 10^{-4}, 847.56, 2.22]$.

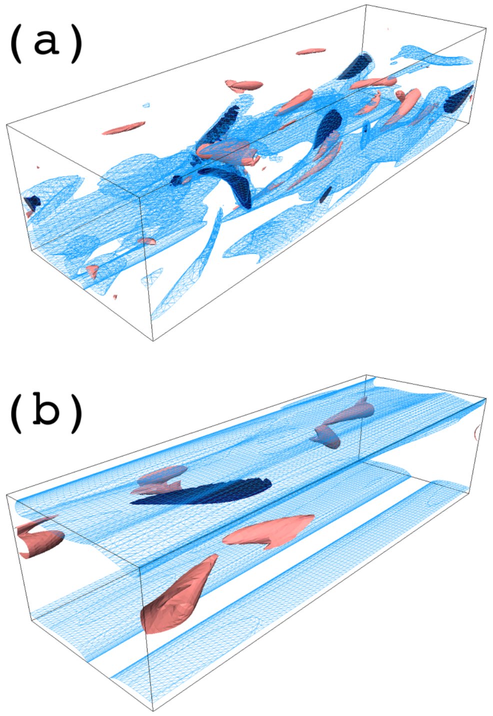

FIG. 10. Isosurfaces of Q (pink solid), $\mathrm{tr}(\boldsymbol{\alpha})$ (light blue meshed), and $\alpha_{yy}+\alpha_{zz}$ (dark blue translucent) for typical active and hibernating instants in the regular DNS ($\mathrm{Wi}=28$); the isosurface levels $[Q_{\mathrm{iso}},\mathrm{tr}(\boldsymbol{\alpha})_{\mathrm{iso}},(\alpha_{yy}+\alpha_{zz})_{\mathrm{iso}}]$ used in each instant are different: (a) active $[5.25\times10^{-2},1455.36,1370.65]$ and (b) hibernating $[1.83\times10^{-2},514.78,156.16]$.

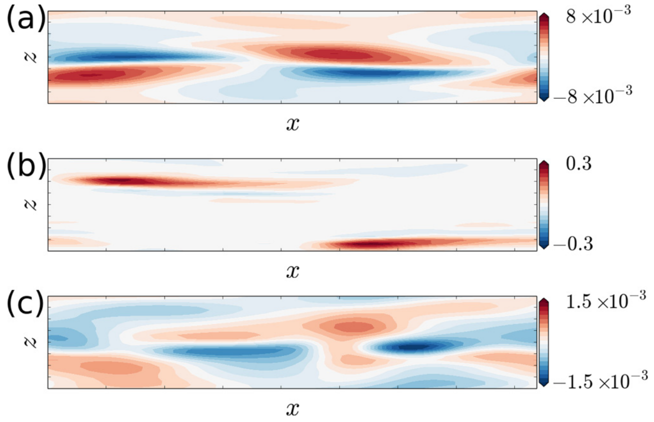

FIG. 11. Distribution of $\hat{Q}$ at $y^+=24.85$ for the three selected instants indicated in Fig. 2: (a) I, (b) II, and (c) III.

Therefore, almost all polymer extension observed in $\mathrm{tr}(\boldsymbol{\alpha})$ (Fig. 7) results from the mean shear. Polymer-turbulence interaction at the ES is minimal, which explains its insensitivity to Wi. (We do however observe that with increasing Wi the period of ES dynamics becomes slightly longer, the reason for which is unclear.)

Similar qualitative features are also observed during the hibernating phase of a regular DNS trajectory [Fig. 10(b)]. The vortex strength, indicated by Q_{iso}, is at the same order of magnitude as instant II of the ES [Fig. 9(b)]. The $\mathrm{tr}(\boldsymbol{\alpha})$ isosurfaces are detached from the vortices, again indicating a predominant contribution from the mean shear. This is in sharp contrast to active turbulence shown in Fig. 10(a). The value of Q_{iso} is much higher than both the ES and hibernating turbulence and so are $\mathrm{tr}(\boldsymbol{\alpha})_{\mathrm{iso}}$ and $(\alpha_{yy}+\alpha_{zz})_{\mathrm{iso}}$. Vortices are much stronger and become more irregularly shaped, with a much shorter length span and more random orientation. Both $\mathrm{tr}(\boldsymbol{\alpha})$ and $\alpha_{yy}+\alpha_{zz}$ isosurfaces wrap around the vortices, showing that in all directions turbulence-induced polymer deformation surpasses that of the mean shear as the main contribution to $\mathrm{tr}(\boldsymbol{\alpha})$.

It is apparent from Eq. (13) that a large positive Q value indicates strong rotational flow, a large negative Q value indicates strong extensional flow, and for shear flow Q is close to zero [77]. Choosing cutoffs between different types of kinematics is however not obvious, especially given the large variations in Q between flow fields. Here we propose a normalized variation of the Q criterion

$$\hat{Q}\equiv\frac{2Q}{\|\boldsymbol{\nabla}\boldsymbol{v}\|^2}. \tag{17}$$

It is easy to show that $\hat{Q}\in[-1,1]$: $\hat{Q}$ is 1 for purely rotational flow and -1 for purely extensional flow; for shear flow $|\hat{Q}|\ll 1$.

Low $\hat{Q}$ prevails at the ES (Fig. 11), indicating shear-dominated flow kinematics. For most of the time, $\hat{Q}\lesssim O(10^{-2})$: Note its magnitudes at I and III and that the III → I span is over 2/3 of a period (Fig. 2). During the RSS burst (II), both extensional and rotational (vortical) motions become appreciable, but rotation is comparatively stronger. The lack of extension at the ES, which is required for strong polymer deformation and polymer-flow interaction, is the direct reason for its insensitivity to polymer effects. Flow fields of active turbulence [Fig. 12(a)] are populated by regions of strong extension and rotation, where $|\hat{Q}|\to 1$. By contrast, in hibernating turbulence [Fig. 12(b)] $\hat{Q}$ drops to the same level as the ES $[O(10^{-2})]$. Quantitative similarities in near-wall flow activities yet again demonstrate the connection between hibernation and the ES (which as seen earlier is not reflected in bulk flow measurements).

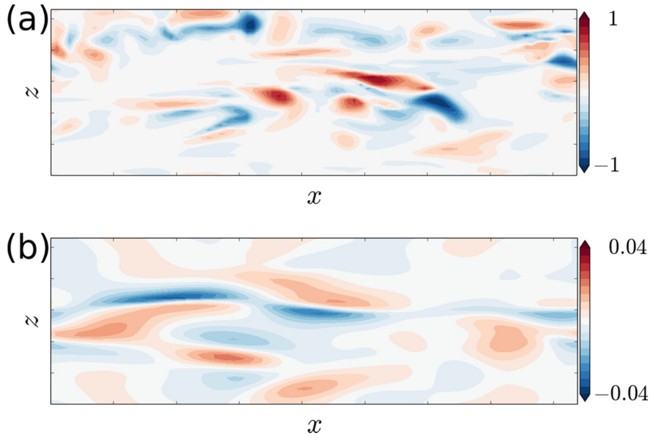

FIG. 12. Distribution of $\hat{Q}$ at $y^+=24.85$ for typical instants in the regular DNS ($\mathrm{Wi}=28$): (a) active and (b) hibernating.

IV. CONCLUSION

Adding to the well-known significance of the ES in understanding the LT transition, evidence is increasingly pointing to its close connection with MDR. Mean flow statistics of the ES are not influenced by polymer effects at least for moderately high Wi [$O(10)$], a result first reported by Xi and Graham [38], but further confirmed here for different domain sizes. This clearly explains why polymer-induced DR must be bounded by an upper limit and why this upper limit is necessarily universal to different polymer solutions.

The dynamics at the ES, both Newtonian and viscoelastic, is dominated by low-frequency (compared with regular DNS) fluctuations. In the more extended domain, it is nearly periodic: Each period includes a quick burst of the RSS followed by a long quiescent period during which the TKE slowly decays. Transitions between periods are accompanied by abrupt shifts of velocity streaks. Flow structures of the ES are localized in both spanwise and wall-normal directions and appear as turbulent spots immersed in a laminar surrounding.

State-space projection of ES trajectories, using coordinates measuring near-wall turbulent activities, shows a close connection with hibernating turbulence: The latter now seems to be intermittent visits by DNS trajectories to certain states on the ES. Similarities between the two are also reflected in flow structures and kinematics. Same as in active turbulence, near-wall coherent structures at these states also feature streamwise velocity streaks flanked by vortices. The vortices are however more aligned in the flow direction, with an elongated shape and very low vortical strength. This paints a generic description of the so-called weak or marginal turbulence. These traits are reminiscent of the so-call lower-branch exact coherent states [78,79]. Kinematic analysis using the normalized $\hat{Q}$ criterion shows that the flow fields are dominated by shear motion. Although high polymer extension [$\mathrm{tr}(\boldsymbol{\alpha})$] is observed, most of it comes from the mean shear. Absence of polymer-turbulence interaction seems to be a universal feature of weak turbulence (ES and hibernation), the key to explaining MDR.

A lingering question is the quantitative origin of the Virk logarithmic law. The ES mean velocity profile varies with the domain size, an inevitable consequence of structural localization. It also scales differently with Re than the Virk asymptote. To explain this seeming contradiction, we note that the experimental state of MDR is not a single turbulent spot but likely a collection of weak turbulent structures spreading across the domain. How their coupling and interaction give rise to the Virk logarithmic law remains an open question. Equally interesting is to find out if and under what conditions the ES can be shifted or suppressed. This will explain the higher-than-Virk level of DR in surfactant solutions [80,81] and also inspire new engineering approaches for turbulent friction control.

ACKNOWLEDGMENTS

The authors are indebted to John F. Gibson (University of New Hampshire) for sharing his CHANNELFLOW code [56] and valuable advice during our program development. Helpful discussion with Bing-Chen Wang (University of Manitoba) is also acknowledged. This work was made possible by financial support from the Natural Sciences and Engineering Research Council of Canada through its Discovery Grants Program (No. RGPIN-2014-04903) and by the facilities of the Shared Hierarchical Academic Research Computing Network (SHARCNET) [82] and Compute/Calcul Canada. Our data processing and visualization benefited from open-source software projects including SCIPY [83], MATPLOTLIB [84], and PARAVIEW [85].

---

[1] J. L. Lumley, Annu. Rev. Fluid Mech. **1**, 367 (1969).
[2] P. S. Virk, AIChE J. **21**, 625 (1975).
[3] M. D. Graham, in *Rheology Reviews 2004*, edited by D. M. Binding and K. Walters (British Society of Rheology, London, 2004), pp. 143–170.
[4] M. D. Graham, Phys. Fluids **26**, 101301 (2014).
[5] C. M. White and M. G. Mungal, Annu. Rev. Fluid Mech. **40**, 235 (2008).
[6] E. De Angelis, C. M. Casciola, and R. Piva, Comput. Fluids **31**, 495 (2002).
[7] Y. Dubief, C. M. White, V. E. Terrapon, E. S. G. Shaqfeh, P. Moin, and S. K. Lele, J. Fluid Mech. **514**, 271 (2004).
[8] Y. Dubief, V. E. Terrapon, C. M. White, E. S. G. Shaqfeh, P. Moin, and S. K. Lele, Flow Turbul. Combust. **74**, 311 (2005).
[9] W. Li, L. Xi, and M. D. Graham, J. Fluid Mech. **565**, 353 (2006).
[10] K. Kim, C. F. Li, R. Sureshkumar, S. Balachandar, and R. J. Adrian, J. Fluid Mech. **584**, 281 (2007).
[11] P.-G. de Gennes, *Introduction to Polymer Dynamics* (Cambridge University Press, Cambridge, 1990).
[12] V. S. L'vov, A. Pomyalov, I. Procaccia, and V. Tiberkevich, Phys. Rev. Lett. **92**, 244503 (2004).
[13] W. B. Giles and W. T. Pettit, Nature (London) **216**, 470 (1967).
[14] A. A. Draad, G. D. C. Kuiken, and F. T. M. Nieuwstadt, J. Fluid Mech. **377**, 267 (1998).
[15] M. P. Escudier, F. Presti, and S. Smith, J. Non-Newton. Fluid Mech. **81**, 197 (1999).
[16] A. Ram and A. Tamir, J. Appl. Polym. Sci. **8**, 2751 (1964).
[17] R. J. Hansen and R. C. Little, Nature (London) **252**, 690 (1974).
[18] J. Kim, P. Moin, and R. Moser, J. Fluid Mech. **177**, 133 (1987).
[19] S. B. Pope, *Turbulent Flows* (Cambridge University Press, Cambridge, 2000).
[20] M. D. Warholic, D. K. Heist, M. Katcher, and T. J. Hanratty, Exp. Fluids **31**, 474 (2001).
[21] C. M. White, V. S. R. Somandepalli, and M. G. Mungal, Exp. Fluids **36**, 62 (2004).
[22] K. D. Housiadas, A. N. Beris, and R. A. Handler, Phys. Fluids **17**, 035106 (2005).
[23] C. F. Li, R. Sureshkumar, and B. Khomami, J. Non-Newton. Fluid Mech. **140**, 23 (2006).
[24] L. Xi, Nonlinear dynamics and instabilities of viscoelastic fluid flows, Ph.D. Thesis, University of Wisconsin–Madison, 2009.
[25] K. R. Sreenivasan and C. M. White, J. Fluid Mech. **409**, 149 (2000).
[26] L. Xi and M. D. Graham, J. Fluid Mech. **693**, 433 (2012).

[27] R. Benzi, E. De Angelis, V. S. L'vov, and I. Procaccia, Phys. Rev. Lett. **95**, 194502 (2005).

[28] I. Procaccia, V. S. L'vov, and R. Benzi, Rev. Mod. Phys. **80**, 225 (2008).

[29] L. Xi and M. D. Graham, Phys. Rev. Lett. **104**, 218301 (2010).

[30] S. N. Wang, M. D. Graham, F. J. Hahn, and L. Xi, AIChE J. **60**, 1460 (2014).

[31] Y. Dubief, C. M. White, E. S. G. Shaqfeh, and V. E. Terrapon, *Annual Research Briefs* (Center for Turbulence Research, Stanford, 2010), pp. 395–404.

[32] S. Tamano, M. D. Graham, and Y. Morinishi, J. Fluid Mech. **686**, 352 (2011).

[33] J. S. Park and M. D. Graham, J. Fluid Mech. **782**, 430 (2015).

[34] J. D. Skufca, J. A. Yorke, and B. Eckhardt, Phys. Rev. Lett. **96**, 174101 (2006).

[35] T. M. Schneider and B. Eckhardt, Chaos **16**, 041103 (2006).

[36] S. Zammert and B. Eckhardt, J. Fluid Mech. **761**, 348 (2014).

[37] B. Eckhardt, T. M. Schneider, B. Hof, and J. Westerweel, Annu. Rev. Fluid Mech. **39**, 447 (2007).

[38] L. Xi and M. D. Graham, Phys. Rev. Lett. **108**, 028301 (2012).

[39] D. Samanta, Y. Dubief, M. Holzner, C. Schäfer, A. N. Morozov, C. Wagner, and B. Hof, Proc. Natl. Acad. Sci. USA **110**, 10557 (2013).

[40] Y. Dubief, V. E. Terrapon, and J. Soria, Phys. Fluids **25**, 110817 (2013).

[41] T. Itano and S. Toh, J. Phys. Soc. Jpn. **70**, 703 (2001).

[42] S. Toh and T. Itano, J. Fluid Mech. **481**, 67 (2003).

[43] T. M. Schneider, B. Eckhardt, and J. A. Yorke, Phys. Rev. Lett. **99**, 034502 (2007).

[44] T. M. Schneider, J. F. Gibson, M. Lagha, F. De Lillo, and B. Eckhardt, Phys. Rev. E **78**, 037301 (2008).

[45] Y. Duguet, A. P. Willis, and R. R. Kerswell, J. Fluid Mech. **613**, 255 (2008).

[46] D. Viswanath, in *Mathematics and Computation, A Contemporary View*, Proceedings of the Third Abel Symposium, edited by H. Munthe-Kaas and B. Owren (Springer, Berlin, 2008), Vol. 3, pp. 109–127.

[47] D. Viswanath and P. Cvitanović, J. Fluid Mech. **627**, 215 (2009).

[48] S. Zammert and B. Eckhardt, Fluid Dyn. Res. **46**, 041419 (2014).

[49] R. B. Bird, C. F. Curtis, R. C. Armstrong, and O. Hassager, *Dynamics of Polymeric Liquids*, 2nd ed. (Wiley, New York, 1987), Vol. 2.

[50] M. Nishioka and M. Asai, J. Fluid Mech. **150**, 441 (1985).

[51] R. Peyret, *Spectral Methods for Incompressible Viscous Flow* (Springer, New York, 2002).

[52] R. Sureshkumar and A. N. Beris, J. Non-Newton. Fluid Mech. **60**, 53 (1995).

[53] R. Sureshkumar and A. N. Beris, Phys. Fluids **9**, 743 (1997).

[54] P. K. Ptasinski, B. J. Boersma, F. T. M. Nieuwstadt, M. A. Hulsen, B. H. A. A. van den Brule, and J. C. R. Hunt, J. Fluid Mech. **490**, 251 (2003).

[55] L. Xi and M. D. Graham, J. Fluid Mech. **647**, 421 (2010).

[56] J. F. Gibson, Channelflow: A spectral Navier-Stokes simulator in C++, University of New Hampshire Report, 2014, channelflow.org

[57] J. Jiménez and P. Moin, J. Fluid Mech. **225**, 213 (1991).

[58] B. Hof, J. Westerweel, T. M. Schneider, and B. Eckhardt, Nature (London) **443**, 59 (2006).

[59] N. R. Lebovitz, Commun. Nonlinear Sci. Numer. Simul. **17**, 2095 (2012).

[60] C. R. Smith and S. P. Metzler, J. Fluid Mech. **129**, 27 (1983).

[61] T. M. Schneider, J. F. Gibson, and J. Burke, Phys. Rev. Lett. **104**, 104501 (2010).

[62] A. Agarwal, L. Brandt, and T. A. Zaki, J. Fluid Mech. **760**, 278 (2014).

[63] W. Li and M. D. Graham, Phys. Fluids **19**, 083101 (2007).

[64] M. D. Warholic, H. Massah, and T. J. Hanratty, Exp. Fluids **27**, 461 (1999).

[65] K. D. Housiadas and A. N. Beris, Phys. Fluids **15**, 2369 (2003).

[66] A. de Lozar, F. Mellibovsky, M. Avila, and B. Hof, Phys. Rev. Lett. **108**, 214502 (2012).

[67] X. Wu, P. Moin, R. J. Adrian, and J. R. Baltzer, Proc. Natl. Acad. Sci. USA **112**, 7920 (2015).

[68] T. Min, H. Choi, and J. Y. Yoo, J. Fluid Mech. **492**, 91 (2003).

[69] S. K. Robinson, Annu. Rev. Fluid Mech. **23**, 601 (1991).

[70] M. Hultmark, M. Vallikivi, S. C. C. Bailey, and A. J. Smits, Phys. Rev. Lett. **108**, 094501 (2012).

[71] F. Waleffe, Phys. Rev. Lett. **81**, 4140 (1998).

[72] H. Faisst and B. Eckhardt, Phys. Rev. Lett. **91**, 224502 (2003).

[73] B. Hof, C. W. H. van Doorne, J. Westerweel, F. T. M. Nieuwstadt, H. Faisst, B. Eckhardt, H. Wedin, R. R. Kerswell, and F. Waleffe, Science **305**, 1594 (2004).

[74] H. Wedin and R. R. Kerswell, J. Fluid Mech. **508**, 333 (2004).

[75] J. Jeong and F. Hussain, J. Fluid Mech. **285**, 69 (1995).

[76] Y. Dubief and F. Delcayre, J. Turbul. **1**, 1 (2000).

[77] J. C. R. Hunt, A. A. Wray, and P. Moin, *Proceedings of the Summer Program* (Center for Turbulence Research, Stanford, 1988), pp. 193–208.

[78] F. Waleffe, J. Fluid Mech. **435**, 93 (2001).

[79] J. Wang, J. F. Gibson, and F. Waleffe, Phys. Rev. Lett. **98**, 204501 (2007).

[80] H. W. Bewersdorff and D. Ohlendorf, Colloid Polym. Sci. **266**, 941 (1988).

[81] Z. Chara, J. L. Zakin, M. Severa, and J. Myska, Exp. Fluids **16**, 36 (1993).

[82] SHARCNET, available at www.sharcnet.ca

[83] E. Jones, T. Oliphant, P. Peterson *et al.*, SciPy: Open source scientific tools for PYTHON, 2001.

[84] J. D. Hunter, Comput. Sci. Eng. **9**, 90 (2007).

[85] U. Ayachit, *The ParaView Guide: A Parallel Visualization Application* (Kitware, Inc., Clifton Park, 2015).